Detailed Analysis of the Velocity Fields from 60 kW Swirl-Stabilized Coal Flames in CO$_2$/O$_2$- and N$_2$/O$_2$-Atmospheres by Means of Laser Doppler Velocimetry and Particle Image Velocimetry

D. Zabrodiec , L. Becker, J. Hees, A. Maßmeyer, M. Habermehl, O. Hatzfeld, A. Dreizler & R. Kneer

Published online: 30 Jun 2017.

Submit your article to this journal

Article views: 24

View related articles

View Crossmark data

Taylor & Francis
Taylor & Francis Group

Check for updates

Detailed Analysis of the Velocity Fields from 60 kW Swirl-Stabilized Coal Flames in CO_2/O_2- and N_2/O_2-Atmospheres by Means of Laser Doppler Velocimetry and Particle Image Velocimetry

D. Zabrodiec [a], L. Becker[b], J. Hees[a], A. Maßmeyer[a], M. Habermehl[a], O. Hatzfeld[a], A. Dreizler[b], and R. Kneer[a]

[a]Institute of Heat and Mass Transfer, RWTH Aachen University, Aachen, Germany; [b]TU-Darmstadt, Reaktive Strömungen und Messtechnik, Darmstadt, Germany

ABSTRACT

This work presents experimental results from flow field measurements of swirl stabilized pulverized-coal flames in oxy-fuel conditions and in conventional atmospheres to characterize the influence of the mixture upon flame aerodynamics. Experiments were carried out on flames inside a cylindrical combustion chamber equipped with a pulverized-coal swirl burner. Flow fields for different flame configurations were measured by means of laser Doppler velocimetry (LDV) and are complemented by particle image velocimetry (PIV). The experimental setups and results are presented, compared, and discussed. LDV measurements provide radial profiles for mean and RMS axial and tangential velocity components at different cross sections inside the combustion chamber. PIV measurements provide planar two-dimensional flow field information about mean values for the axial and the radial velocity components of the flow, as well as qualitative information about solid particle distribution inside the combustion chamber. The performance of LDV and PIV as optical measurement techniques is evaluated for the present case. Coal particles with a wide size distribution are used as flow tracers in the experiments. The influences of particle size upon obtained results, the measured flow fields, and qualitative particle distributions are discussed in detail.

Introduction

The share of electricity and heat generated by coal in the world is around 40% and it has been similar for the last 40 years (IEA, 2016). Given the rate of population and economic growth of developing nations, coal, as one of the cheapest and most abundant energy sources, will continue being one of the primary energy sources for many years to come. The reduction of CO_2 atmospheric emission from hydrocarbon combustion has, for many years now, been the most important challenge for the energy industry and scientific community. In order to target this challenge, oxy-fuel combustion was proposed

---

CONTACT Diego Zabrodiec ✉ zabrodiec@wsa.rwth-aachen.de 🖅 Institute of Heat and Mass Transfer (WSA), RWTH Aachen University, Augustinerbach 6, Aachen DE-52056, Germany.

Color versions of one or more of the figures in the article can be found online at http://www.tandfonline.com/gcst.

(Abraham et al., 1982) as an alternative technology to reduce CO_2 emissions by improving the efficiency of carbon capture and sequestration (CCS) processes.

In oxy-fuel combustion, the fuel is burned in oxidizing atmospheres composed mainly of O_2/CO_2 mixtures. At power plant scales, particularly for pulverized coal, this can be achieved by recirculating the flue gas and mixing oxygen with it. Advantages for this technology are multiple: (i) Flue gas produced by using recirculated flue gases and oxygen is mainly composed of CO_2, which can be almost directly compressed and captured underground (Chen et al., 2012). (ii) Existing coal power plants can be retrofitted with the technology. (iii) The replacement of N_2 by CO_2 in the oxidant combined with the possibility of selecting the oxygen concentration can be used to control flame temperatures, thus reducing the production and emission of NO_x and other pollutants (Chen et al., 2012). In depth information about fundamentals of oxy-fuel combustion and recent experimental and numerical works can be found in reviews (Chen et al., 2012; Croiset et al., 2005; Scheffknecht et al., 2011; Wall et al., 2009). In addition, information about the state of the art of CCS with oxy-fuel combustion can be found elsewhere (Cuéllar-Franca and Azapagic, 2015; Leung et al., 2014). The development of oxy-fuel combustion technology is currently at a stage of rapid advance, although it is a complex process, involving research in different fields. New advances in modeling and increasing complexity in numerical simulations are pushing the technology forward towards commercialization. Nevertheless, despite these advances, experimental data from pulverized coal combustion in atmospheric and oxy-fuel conditions is scarce. For that reason, more experimental data is needed to fill the gaps in modeling, as well as for the verification and validation of computational numerical models.

Laser Doppler velocimetry (LDV) and particle image velocimetry (PIV) are laser-based, optical measurement techniques commonly used for the characterization of reactive flow fields. Both techniques rely on laser light scattered by tracer particles present in the flows (Albrecht et al., 2003). LDV provides point measurements of single velocity components while PIV provides planar, two component velocity measurements. Advantages and disadvantages from both techniques are complementary and dependent on the application case. More detailed information about the techniques can be found in Albrecht et al. (2003) and Tropea et al. (2007). Optical access to the flow is a primary requirement for the successful application of these techniques. Unfortunately, in the case of coal-fired boilers, optical access is usually difficult or even impossible. The experimental configuration employed in this work corresponds to a combination of concentric annular swirling and non-swirling jets. This experimental configuration can generate flow conditions that resemble those found in practical coal-fired boilers. Swirling flows are difficult to compute given their complex structure. Therefore, measurement data, as the one currently presented, is valuable to improve the understanding of the complex mechanisms involved in pulverized coal combustion and to validate numerical simulations.

Flow fields in pulverized coal flames have previously been studied by measuring coal particle velocities. Pröbstle and Wenz (1988) proved the applicability of LDV measurements upon coal flames and performed measurements on a 0.8 MW pulverized coal swirl flame. Abbott (1989) performed LDV measurements on 0.5 MW pulverized coal flames. Weber et al. (1992) measured particle velocities of a 2.5 MW flame in the IFRF (International Flame Research Foundation) Furnace No. 1 and discussed the errors given by coal particle slip when used as flow tracers. Ereaut and Gover (1991) measured

particle velocities from a 37 MW flame using a water-cooled LDV probe. Schnell et al. (1993), Jensen et al. (1994), and Pickett et al. (1999) also performed LDV measurements in smaller pulverized coal flames and discussed the errors introduced by coal particle slip in detail. The flow fields from pulverized coal flames in oxy-fuel atmospheres have been characterized only recently: Toporov et al. (2008) performed LDV measurements upon a different set of flames in the present combustion chamber; Heil et al. (2009) studied the aerodynamic performance of different burner designs under oxy-fuel conditions by LDV, and Weidmann et al. (2015) conducted LDV measurements in a combustion chamber for the pulverized coal flameless oxidation process (FLOX).

Given the optical access limitations in many practical and pilot-scale pulverized coal flames, PIV measurements on pulverized coal flames are still rare. El Gendy et al. (2010) performed PIV measurements upon a laboratory-scale laminar pulverized coal-methane flame. Fielenbach et al. (2003) performed PIV measurements to evaluate the characteristics of the near burner aerodynamics, of a pulverized coal flameless oxidation process (FLOX) in a pressurized reactor. More recently, Balusamy et al. (2013) performed PIV measurements with unprecedented detail upon laboratory-scale swirl coal-methane flames in atmospheric and oxy-fuel conditions. Results were also compared with LDV measurements and the error in coal particle as tracers was discussed. Sung et al. (2016) also performed PIV measurements on similar laboratory-scale swirl coal-methane flames in order to study the impact of the internal recirculation zone aerodynamics on NO_x reduction.

This study contributes with the flow field characterization of three different pulverized coal swirl flames, one conventional air-fired, and two oxy-fuel cases. Flow field characterization is achieved by LDV (two-component) measurements complemented by PIV measurements. Qualitative in-flame solid particle distributions obtained from the PIV images are also presented and discussed. Furthermore, detailed information is provided about the implementation of the measurement techniques as well as data acquisition and evaluation. Flow fields and particle distribution results are presented and discussed to describe the effects of the chosen study cases upon flame structure and behavior.

Experimental setup

Test facility and operating conditions

Measurements were carried out at the WSA-RWTH Aachen University combustion test furnace. It is composed of a cylindrical, vertically mounted, down-fired combustion chamber with an internal diameter of 400 mm and a maximal height of 4200 mm (cf. Figure 1). The top section of the combustion chamber, so called burner port, is made of ceramic material and the burner is mounted in its center. This burner port can be accurately traversed along the axis of the combustion chamber. The inner walls of the combustion chamber are formed by three layers of ceramic insulation with electric heating elements embedded in the most external layer. The heating elements serve to raise wall temperatures up to a range of 800°C to 1000°C. Wall temperatures are monitored by embedded thermocouples in the ceramic material; also, the inner-surface temperatures can be obtained by means of two-color pyrometry (Hees et al., 2016b). The combination of both ceramic material and electric heating minimizes heat losses and allows the
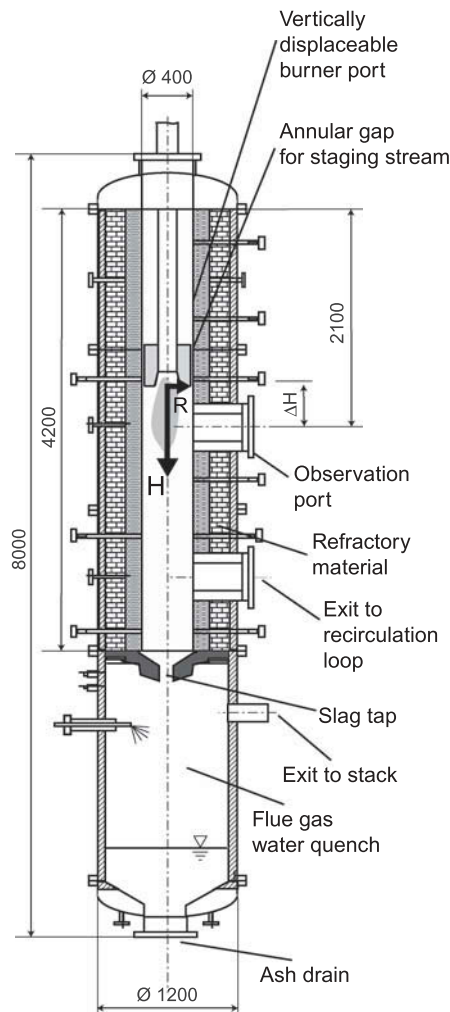
Figure 1. Longitudinal cut of the test combustion chamber showing most important dimensions and characteristics.

operation of the combustion chamber at almost uniform temperatures for different operating conditions and thermal loads.

At the half length (2100 mm, cf. Figure 2) of the combustion chamber, three radial observation ports are available for probe and optical measurements. Two ports provide optical access to the flame, while the third port is used for probe access (not used in this study). All three ports have a clear aperture diameter of 100 mm to the combustion chamber.

The traversable burner (cf. Figure 3) was designed to aid the stable combustion of pulverized coal in oxy-fuel low oxygen concentration atmospheres (Habermehl et al., 2012; Heil et al., 2009; Toporov et al., 2008). It is formed by two concentric annular orifices (cf. Figure 3). The expansion of the gases ejected by these two orifices is restricted by a conical quarl with an exit diameter of $D_q = 120$ mm (quarl angle, $a = 27.76°$). The
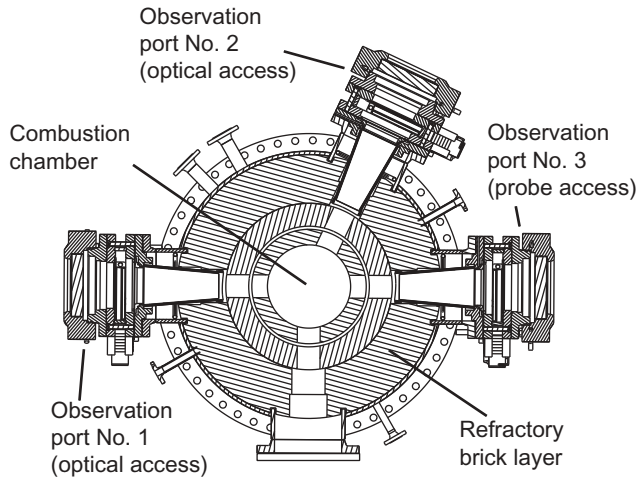
Figure 2. Transversal cut of the test combustion chamber at the level of the observation port, ports 1 and 2, provide optical access.
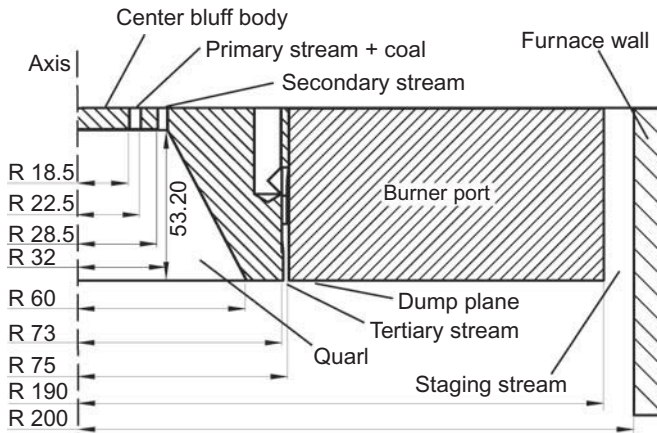

Figure 3. Half section of the swirl burner mounted at the burner port, dimensions given in mm.

level where the gases leave the quarl (dump plane) is coincident with the burner port. The central annular orifice (hydraulic diameter $D_{H1} = 8$ mm), named primary, is built around a central bluff body and provides the premixed fuel-oxidant mixture. The adjacent annular orifice (hydraulic diameter $D_{H2} = 7$ mm), named secondary, provides a swirled oxidizer stream. Swirling of the secondary stream is produced inside the body of the burner (upstream) in a mixing chamber. Two additional annular orifices also provide oxidizer, the tertiary stream and the staging stream (with hydraulic diameters of $D_{H3} = 4$ mm and $D_{HS} = 20$ mm, respectively). The former is located at the level of the dump plane between the quarl and the burner port, and the latter is located at the gap between the burner port and the walls of the chamber (width approximately 10 mm, cf. Figure 1). Both streams have the purpose of staging the flame and diluting the product gases at regions downstream from the flame.

Coal particles are fluidized into the primary stream by means of a twin-screw volumetric feeder combined with a venturi-type ejector. This allows a controlled and continuous coal particle flow into the combustion chamber. Oxidant gas supply is controlled by electronic mass flow controllers with typical accuracy of 1% or higher for the chosen flow rates.

Operating conditions

Three test cases were chosen to study the effects of the oxidizer's composition upon flame flow fields: two oxy-fuel cases and one conventional air-fired reference, which are based on previous results obtained (Habermehl et al., 2016; Hees et al., 2016a). These operating conditions have shown good stability and well-defined flame structures and have comparable characteristics to the operating conditions studied at other similar test facilities (Andersson and Johnsson, 2007; Liu et al., 2005; Silva et al., 2014; Wang et al., 1988).

Table 1 shows all relevant parameters for all three studied operating conditions. The thermal output of the flame was kept constant in all three studied cases at 60 kW. Volume flow rate for the primary stream was also fixed in all cases in order to keep the injection velocity of coal particles into the combustion chamber constant. Only oxidizer

Table 1. Operating conditions.

Parameter		AIR	OXY21	OXY25
Coal mass flow	[kg/h]	9.8	9.8	9.8
Volume flow rate of primary stream[a]	[m³/h]	9.4	9.4	9.4
O_2 fraction of primary stream	[vol%]	19	19	20.2
N_2 or CO_2 fraction of primary stream[b]	[vol%]	81	81	79.8
Temperature of primary stream	[°C]	25	25	25
Volume flow rate of secondary stream[a]	[m³/h]	28.8	28.8	23.8
Volume flow rate of tertiary stream[a]	[m³/h]	5.1	5.1	4.2
Volume flow rate of staging stream[a]	[m³/h]	26.5	26.5	22.2
O_2/CO_2 composition of secondary, tertiary and staging stream[b]	[vol%]/[vol%]	21/79	21/79	25/75
Swirl number of secondary stream		0.95	0.95	0.95
Temperature of secondary stream	[°C]	40	40	40
Temperature of tertiary stream	[°C]	40	40	40
Temperature of staging stream[c]	[°C]	900 ± 10	900 ± 10	900 ± 10
Global oxygen-fuel ratio[a] (λ_{global})	[–]	1.3	1.3	1.3
Local oxygen-fuel ratio[a] (λ_{local})	[–]	0.8	0.8	0.8
Bulk velocity primary stream[a] (U_I)	[m/s]	5.07	5.07	5.07
Bulk velocity secondary stream[a] (U_{II})	[m/s]	12.07	12.07	10.29
Bulk velocity tertiary stream[a] (U_{III})	[m/s]	1.52	1.52	1.25
Bulk velocity staging stream[e] (U_{ST})	[m/s]	2.58	2.58	2.16
Reynolds no. primary stream[d]	[–]	2574.27	4317.41	4219.77
Reynolds no. secondary stream[d]	[–]	4902.84	8165.64	6768.94
Reynolds no. tertiary stream[d]	[–]	353.68	591.10	476.29
Reynolds no. staging stream[d]	[–]	697.41	1165.56	955.38
Momentum flux primary stream	$[kg\,m/s^2] \cdot 10^{-3}$	15.20	20.74	20.41
Momentum flux secondary stream	$[kg\,m/s^2] \cdot 10^{-3}$	111.31	150.76	106.49
Momentum flux tertiary stream	$[kg\,m/s^2] \cdot 10^{-3}$	2.48	3.38	2.26
Momentum flux staging stream	$[kg\,m/s^2] \cdot 10^{-3}$	5.08	6.93	4.79

[a]STP = Standard temperature (0°C) and pressure (1,013 bar).
[b]For the AIR combustion case, shown percentages correspond to the ratio of O_2/N_2.
[c]Geometrical swirl numbers, given by the geometry of the burner.
[d]Reynolds no. calculated from bulk velocities and the hydraulic diameters of both nozzles.
[e]Calculated for a temperature of 900°C and pressure of 1,013 bar.

composition was modified between a conventional atmospheric reference case (AIR) and two-oxy fuel cases, one with 21 vol% O_2 and 79 vol% CO_2 (OXY21) and another with 25 vol% O_2 and 75 vol.% CO_2 (OXY25). The geometric swirl number for all conditions is $S_g = 0.95$, calculated from the geometry of burner and the definition given by Chigier and Beer (1964b). Flame stoichiometry is kept constant for all studied cases. The operation of the present combustion chamber can be described by two oxygen-fuel ratios: the first is the global ratio λ_{global}, the ratio between the total oxygen provided to the combustion chamber and the one needed for the full combustion of the fuel provided. The second, the local ratio λ_{local}, is the one computed from the oxygen provided through the burner to the amount of oxygen needed for complete combustion, excluding the staging air. All studied cases share the common oxygen fuel ratios $\lambda_{global} = 1.3$ and $\lambda_{local} = 0.8$. The adopted configuration provides an overall lean oxygen-gas mixture to the chamber with a fuel-rich zone in the proximity of the burner. The concentration of O_2 in the primary stream was set to be less than 21 vol% as a safety measure, to avoid ignition of coal particles inside the supply lines (cf. Table 1). The fuel used in this study was Rhenish Lignite (RBK); coal composition and heating values obtained from the ultimate analysis are given in Table 2. Particle size distribution is presented in Figure 4. The estimated percentile diameters are $D_{10} = 5.61$ μm, $D_{50} = 29.67$ μm, and $D_{90} = 132.62$ μm. The coal particle relaxation time corresponding to the median size (29.67 μm) in the most unfavorable case (OXY21 with the smallest dynamic viscosity) is $\tau_0 = 2.82$ ms.

Measurement techniques

Flow field measurements were carried out by means of LDV and complementary PIV. Both methods are based on optical diagnostics and rely on the presence of tracer particles in the flow; therefore, the magnitude of the error in the measurements strongly depends on how well the tracer particles follow the flow. Measurements presented in this work are based completely on the use of coal particles as flow tracers. Coal particle Stokes number, estimated from the hydraulic diameter and the bulk velocity of the secondary streams, and chosen as representative parameters of time and length scales of the flows is $S_k = 3.52$ (from an estimated possible range of $S_k \approx 0.09$ for D_{10} to $S_k \approx 100$ for D_{90}), rendering a large number of the coal particles unable to perfectly follow the flow in the presence of high velocity gradients. As shown in the previous section, coal particles in the flame have a

Table 2. Ultimate analysis of pre-dried lignite (RBK).

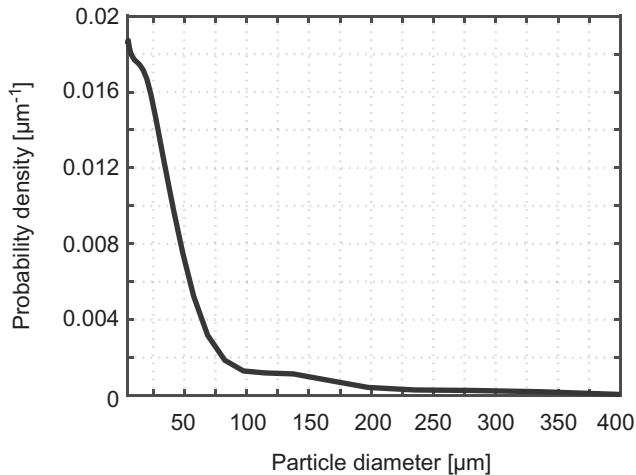| Component		As received	Dry	Dry, ash free
Carbon	[w %]	56.90	64.77	69.05
Hydrogen	[w %]	3.98	4.53	4.83
Oxygen (as difference)	[w %]	20.71	23.57	25.13
Nitrogen	[w %]	0.57	0.65	0.69
Sulfur	[w %]	0.25	0.28	0.30
Water	[w %]	12.15	—	—
Ash	[w %]	5.44	6.19	—
Volatile content	[%]	42.42	48.29	51.47
Lower heating value	[MJ/kg]	20.995	24.237	25.837
Higher heating value	[MJ/kg]	22.153	25.217	26.881

Figure 4. Coal particle size distribution, RBK.

wide particle size distribution, and a large proportion of them does not qualify as reliable gas phase velocity tracers.

Therefore, the design of the LDV-setup has been optimized to minimize the velocity error from particle slip by maximizing the velocity data collected from smaller particles. Radial velocity profiles for the axial and tangential component are obtained from the LDV measurements at different distances from the burner. Two-dimension vector fields (axial and radial velocity components) and qualitative spatial distribution maps of solid particles are obtained by means of PIV measurements. Given the construction of the combustion chamber, velocities cannot be measured at intra-quarl locations; minimum achievable distances for LDV measurements are at 25.6 mm downstream from the dump plane. PIV measurements can be made all the way up to the dump plane but the collected signal in the proximity of the burner has a low signal-noise-ratio (SNR) due to laser scattering at the burner port and due to ash deposits; also, measurements are affected by location with high particle densities.

Laser Doppler velocimetry

LDV measurements were carried out by means of a custom-made long-range sending-receiver optic-system (ILA Laser systems). The system is configured as dual-beam (two-component) with backscatter detection as shown in Figure 5. The operating wavelengths are 488 nm (axial component) and 514.5 nm (tangential component); the source beams are produced by individual optically pumped semiconductor laser heads (Coherent Genesis CX SLM-Series). Each laser head has a CW output of 2 W; the laser beams are guided by means of high-efficiency mirrors. Bragg cells (frequency shifting) are also employed. No optical fibers are used as all the optical components including the laser heads are integrated in a single sending-receiving unit. The custom design of the system allows an improvement of the geometry of the measurement volume. This, combined with the high laser power, leads to a dramatic increment of laser energy flux through the
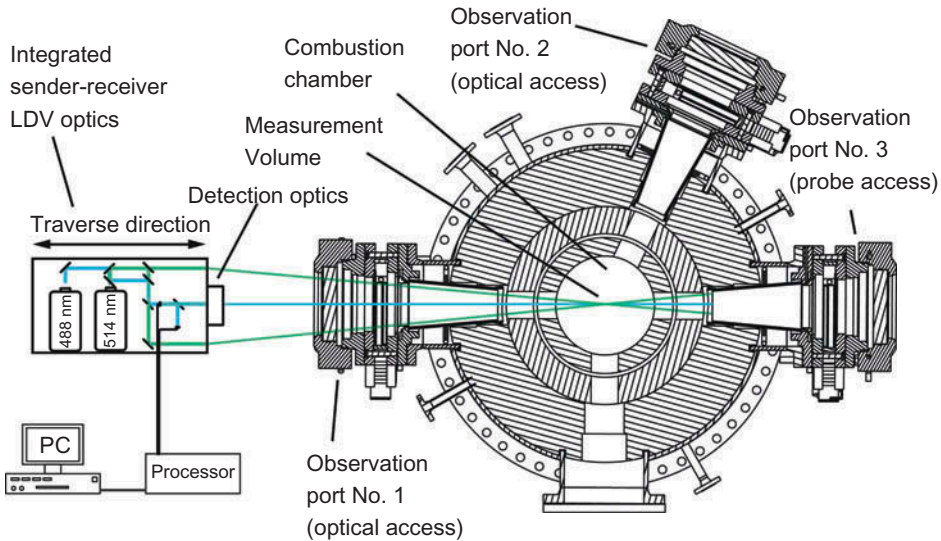
Figure 5. Transversal chamber cut with LDV system layout.

measurement volume, thus increasing the scattering signal levels given by the tracer particles.

The LDV unit is mounted on a traverse system (along the radial coordinate of the chamber) outside observation port no. 1 (cf. Figure 5). Each of the four beams employed has 700 mW of power and all are focused on the measurement volume at a distance of 1750 mm from the sending optics. The beam pair dedicated to the measurement of the axial component (488), produces an ellipsoidal measurement volume with an approximate diameter of $d_{488} = 135$ μm and a length of $L_{488} = 1600$ μm. The beams corresponding to the tangential component (514.5) produce a measurement volume with a diameter of $d_{514} = 150$ μm and a length of $L_{514} = 1800$ μm. Burst signals are collected in back-scatter arrangement through a set of lenses (85 mm diameter) focused on the measurement volume (~1600 mm from the first optical receiver element). Collected burst signals are then separated by a beam splitter and guided by fiber optics to photomultiplier tubes. A LDV burst signal processor (Dantec BSA P80) is employed to control the photomultiplier tubes and to condition and process the raw burst signals. As the number density of coal and ash particles changes at different locations inside the chamber, the voltage applied to photomultipliers was varied, between 900 V and 1200 V. Collected signals from regions with high particle densities (i.e., at the proximity of the burner and close to the chamber axis) presented higher noise levels and were prone to detector saturation; lower voltages were used in these regions. The burst validation ratio in the processor was set to 10, in an attempt to reject the burst signals from larger particles (Balusamy et al., 2013), this validation ratio compares the first and the second peaks in the burst signal spectrum, filtering out the large particles or overlapped signals when multiple particles are present in the measurement volume. Acquisitions on each measurement point were done for 60 s (long enough to include flow fluctuations of all scales, including possible large-scale fluctuations). This, combined with lower photomultiplier voltages and moderate amplification of the burst signal by 22 dB, provided Doppler bursts with high SNR, which kept data rates at values of between 1000 to 8000 counts per

second. Between 50,000 and 100,000 burst counts were collected at each point. The large amount of collected burst counts per measurement point allowed the resulting mean and root mean square (RMS) velocity values to have at least 95% statistical confidence. Transit time weighting for the mean and RMS velocity estimation was included to correct the velocity bias from nonuniform coal particle distributions, typical for turbulent flows.

In order to correct any error introduced by misalignment or inaccurately measured angles between the laser beams, the system was calibrated using a rotating disk (Optolution—ILA LDV velocity standard). For a 10 m/s reference velocity, the LDV system measured velocity values with 0.1% error.

Particle slip velocity error

As described in the section "measurement techniques", the estimated Stokes number for median-sized coal particle (29 μm) is around $S_k = 3.52$ (relaxation time of $\tau_0 = 2.82$ ms); therefore, coal particles are not good flow tracers. Nevertheless, a very large percentage of the particles was measured (by laser diffraction analysis) to be smaller than 29 μm (50%). Several studies where LDV-measurements were carried out on similar scale flames (Jensen et al., 1994; Pickett et al., 1999) have shown a good tracer behavior of coal particles, even for wider size distributions and higher velocities. In these studies, slip-associated errors only appeared in particular regions (i.e., in the immediate vicinity of the burner nozzles or at regions with large velocity gradients). Jensen et al. (1994) experimentally determined that, for coal with a median size of 50 μm, the velocity error given by particle slip was around 10%. Similar results obtained by Pickett et al. (1999) found errors in the order of 3% to 7%, depending on the turbulence level of the flow. The authors also showed that, in conventional theoretical analysis, particle slip is overpredicted as hot combusting gases have much higher viscosities and the actual number density of very small particles is higher than the apparent values. Consequently, the probability of measuring small particles is significantly increased (Schnell et al., 1993).

In an attempt to improve the quality of the acquired data, besides the LDV system optimization for smaller particles, complementary seeding was also tested. Aluminum oxide (Martoxid MR-72, mean diameter ≈ 1 μm) particles were seeded into the secondary stream as a complement to coal particles. Obtained results only showed a small data rate increment but had no effect on mean and RMS values from the measured velocities.

An interesting approach to evaluate how accurately measured coal particles describe the gas flow is by the analysis of velocity fluctuation histograms. Pickett et al. (1999) described that, in flows where large coal particle slip is present, the velocity histograms deviate from the theoretical normal distributions given by a turbulent flow (Pope, 2000). The particle slip can lead instead to bimodal velocity distributions, or produce discontinuities or isolated peaks in the histograms. Figure 6 shows the velocity histograms for the measured axial and tangential velocity component (OXY21 case) at the coordinates $H = 1d$, $R = 78$ μm, location where the maximum axial velocity was measured. These obtained turbulent velocity distributions are smooth, with no indications that significant particle slip is affecting the measurements.

In the present study, a simple analysis was performed in order to predict the effect of particle slip on the measured mean velocities and the turbulent velocity distributions. LDV data was simulated using the Benchmark Generator III code developed by Nobach (2001), with turbulent flow conditions similar to those measured inside the combustion chamber
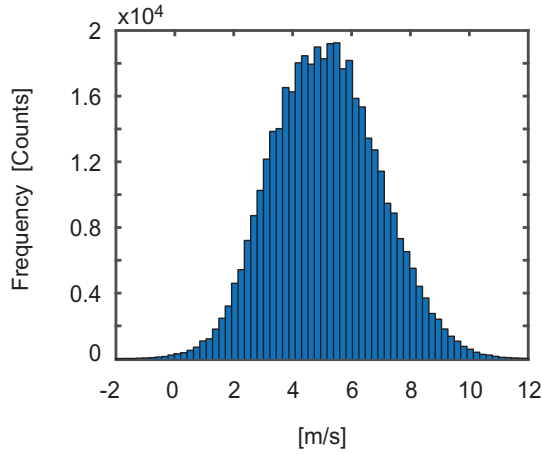
(a) Axial velocity component
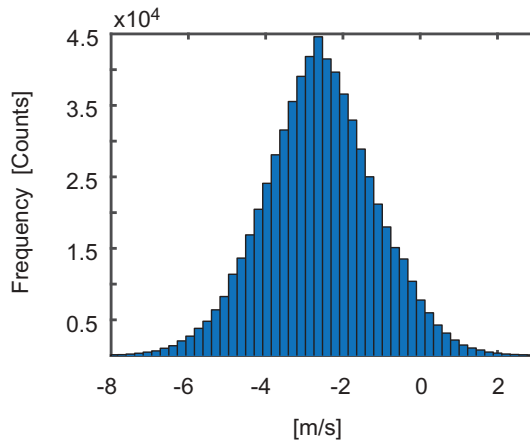
(b) Tangential velocity component

Figure 6. Velocity histograms for OXY21 case, measured by LDV at $H = 1d$ and $R = 78$ mm.

(mean velocity $\bar{u} = 12$ m/s, fluctuation amplitude $u' = 3$ m/s, with a Heisenberg-type spectrum for the turbulent fluctuations). The simulated data, a turbulent velocity time series, with a length of 100,000 samples was used in combination with a randomly generated particle diameter population, with the same size distribution as the one in Figure 4. To estimate the particle-gas velocity slip from an approximation of the Basset–Boussinesq–Oseen equation (Tropea et al., 2007):

$$s = u_p - u_f = d_p^2 \frac{(\rho_p - \rho_f)}{18\mu} \frac{du_p}{dt} \tag{1}$$

Here, s is the particle slip, d_p the diameter of a particle, μ the dynamic viscosity of the flow, u_p, ρ_p and u_f, ρ_f are the velocity and density of the gas and particle phase. The slip value was calculated for the combination of random particle size and velocity using the entire simulated velocity population and randomly added or subtracted from the corresponding simulated velocity sample. Figure 7 shows the velocity histograms from the simulated data and the slip
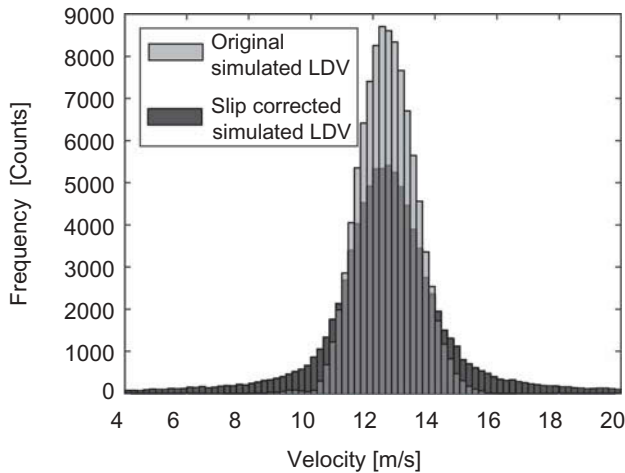
Figure 7. Velocity distributions of simulated LDV data, with and without particle slip.

corrected simulated velocity data. Results show that the main effect of the particle slip lies in the broadening of the velocity distributions. No significant shift on the mean values of the distribution is observed; the values for the mean velocities only differ around 2%. Nevertheless, as the velocity distribution is broader in the slip corrected population, RMS values can be over predicted, with a difference of 40% between the two populations. The estimated values in this section and the compared values obtained by other authors show that despite the fact that coal particles are not ideal tracers, good results can be obtained applying the LDV technique. The large number of small particles which follow the flow very closely combined with the flow fluctuations experienced in the present study have a dominant effect in the statistics over the results given by larger particles.

Particle image velocimetry

To complement the LDV measurements standard two-dimensional PIV was performed using coal particles as tracers. The setup of the PIV measurement system is shown in Figure 8. The beam of a double-pulsed frequency-doubled Nd:YAG laser (New Wave Gemini), with an output wavelength of 532 nm, passed through focusing optics (–50 mm cylindrical and 1000 mm spherical lenses) to form a light sheet. The laser sheet had a thickness of 0.85 mm. The time separation between laser pulses (Δt) ranged from 50 μs for measurements directly downstream of the quarl to 300 μs for measurements at the field of views (FOV) far downstream.

As detector, an sCMOS camera (LaVision, imager sCMOS, 2560×2160 pixels, and 16bit) was used operating at a repetition rate of 2.5 Hz. A 180 mm Sigma macro lens set to f/16 was used resulting in an FOV of 120 mm × 90 mm. Due to the window setup of the combustion chamber, the lens was oriented relative to the measuring plane at an offset angle of $\theta = 30°$ from the normal (cf. Figure 8). To keep the laser sheet in focus a Scheimpflug adapter at an angle of 4.7° was used. Raw images were previously calibrated in the cold combustion chamber using a 2D dotted target (2.5 mm dot diameter, 9.5 mm dot spacing), which was mounted on the center line of the burner.
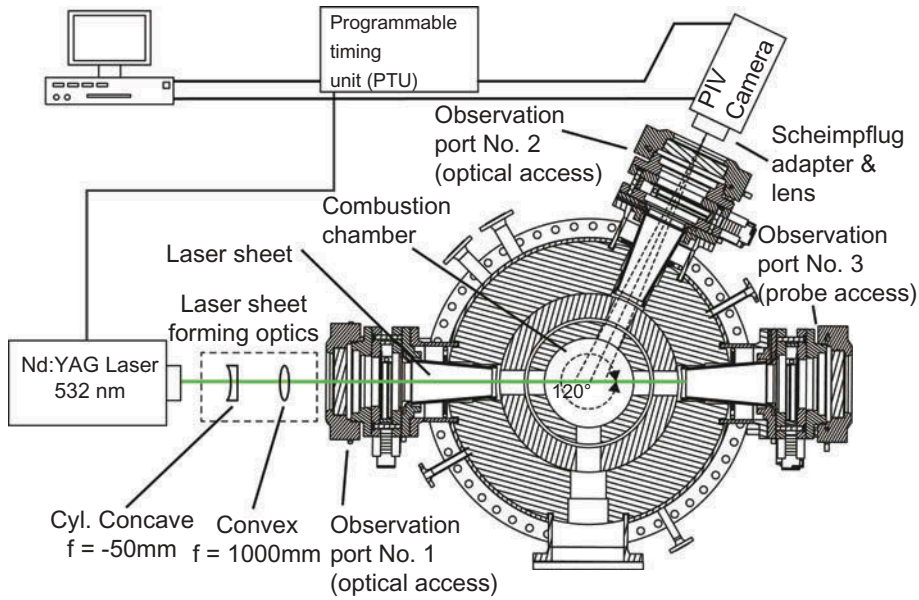
Figure 8. Transversal chamber cross section with PIV system layout.

For data recording and processing the software DaVis (LaVision) was used. All Mie-scattering image pairs were pre-processed before cross correlation by subtracting a sliding average over 64 pixels to reduce noise from soot radiation. The correlation window size was decreased from 128×128 pixels to 64×64 pixels with 75% overlap and two passes. Spurious vectors were detected and eliminated using a Q-Factor of 1.3. The resulting vector field was median-filtered with a filter size of 3×3 vectors. Vectors were removed if they differed more than three standard deviations from the mean of neighboring vectors. The final interrogation window size was 2.8 mm. At each operation point and for each field of view 1000 images were recorded. For most interrogation volumes, between 50% and 80% of the vectors were plausible and available for calculating mean and RMS values. For the region at the edge of the burner quarl this number dropped to approximately 30% due to the increased particle density at this location. Spurious vectors leading to gaps in the velocity fields were usually caused by dense clouds of fine coal particles. These areas are prone to systematic errors (see the "PIV velocity measurements and Mie scatter analysis" section). In the raw images, larger particles that move opposite to the particle cloud in the background can be observed close to the central axis. Depending on the scattering intensity of particles relative to the scattering intensity of particle clouds, either the large particles or the particle cloud dominate the cross correlation. Possible effects on the mean values are discussed in detail in the "PIV velocity measurements and Mie scatter analysis" section.

Results and discussion

LDV velocity measurements

Mean velocity profiles and RMS values from the velocity fluctuations were measured at eight axial positions (as multiples of $d = 64$ mm, corresponding to the radius of the

secondary annular nozzle relative to the dump plane (burner port), with the closest and the most distant profiles at 32 mm (0.5 d) and 384 mm (6 d). Measurements in the vicinity of the dump plane are limited to approximately 32 mm from the dump plane as ash deposits build and fall randomly, blocking the path of the laser.

Figure 9 shows measurement results from the AIR case. Mean axial velocity profiles show the presence of two recirculation zones, the most predominant—the internal recirculation zone (IRZ)—located between the center of the combustion chamber (0 mm) and R = 40–60 mm. Also, the effects of a less prominent external recirculation zone (ERZ) can be observed at different heights located outside the main expanding vortex zone of the flow (between R = 95 mm and R = 120 mm). These are particularly well-known features found in swirl flames (Chigier and Beer, 1964b; Weber et al., 1992). The recirculated hot gases induced by the swirl motion of the flow enhance fuel ignition and stabilize the flame.

For the case of the AIR flame, the IRZ is present between 0.5d and 1.5d; it extends around 60 mm from the dump plane. Maximum axial velocities of $\bar{u} = 7.27$ m/s at $H = 0.5d$ and $R = 68$ mm and $\bar{u} = -1.7$ m/s at $H = 1.5d$ are measured in the center of the combustion chamber. A second recirculation zone was measured in the vicinity of the wall ($R = 200$ mm) between 2d and 4d. Local maxima in RMS velocity values for axial and tangential components are observed to be coincident with significant velocity gradients in the flow. Profiles for $H = 0.5d$ to 1.5d show that the largest gradients are located at the boundaries of the IRZ ($R = 6$ mm) and at the external boundary of the expanding vortex ($R = 80$ mm to 120 mm). These two regions are subjected to strong shear layers, as they are the mixing layers between the IRZ and the high velocity incoming gases (secondary stream). High RMS values are also measured at the axis of the combustion chamber, at 0.5d and 1d. In this region the incoming gases from the primary stream interact with the counter flow generated by IRZ, generating high levels of turbulence in the flow. Maximum values of tangential velocities are coincident with the radial positions at which the highest axial velocity gradients are found, for example, the inner jet boundaries of the expanding vortex. This is a common characteristic in vortex fluid motion and has already been observed in pulverized coal swirl-flames (Jensen et al., 1994; Pickett et al., 1999; Toporov et al., 2008). Maximum tangential velocities of $\bar{v} = -2.9$ m/s and $\bar{v} = 3.8$m/s are measured, respectively, at $H = 0.5d$ near the burner and $H = 2d$ where the IRZ ends. The jet corresponding to the staging stream can be measured near the burner port and the chamber walls, from $H = 0.5d$ to $H = 1.5d$ and between $R = 180$ mm and $R = 200$ mm, with $\bar{u} \approx 2$ m/s. Also, velocity measurements in the window cavity are shown ($R = 200$ mm to 215 mm) for reference purposes. Although the staging stream is not seeded, particle count rates are still ≈ 900 counts per second. This could be attributed to the fact that a large number of small char and ash particles are recirculated by the ERZ towards the dump plane, serving as flow tracers.

Results from measurements of the OXY21 and OXY25 cases are presented in Figures 10 and 11. The profiles from axial and tangential velocities show similar flow patterns as the ones observed for the AIR case but with a smooth evolution in the profiles along the axis of the chamber. Measurements from the OXY21 case (cf. Figure 10a) showed higher positive and negative values for the axial velocity components: $\bar{u} = 8.9$ m/s at $H = 0.5d$, and $\bar{u} = -4.4$m/s at $H = 1d$. The IRZ is larger than the one observed in the AIR case: negative axial values are measured from $H = 0.5d$ all the way down to $H = 6d$. The radius of the IRZ initially decreases from $R = 64$ mm at $H = 0.5d$ to $R = 40$ mm at $H = 2d$ and from then it expands monotonically back to around $R = 60$ mm at $H = 6d$. This is a

typical feature of a type 2 swirl flame according to the IFRF categorization (Leuckel and Fricker, 1976). Tangential velocity profiles (cf. Figure 10a) also show similar patterns as in the AIR case, maximum tangential velocity, $\bar{v} = -4.67$ m/s was measured at $H = 1.5d$. The peak values of the tangential velocity and radial location at different axial positions follow the pattern observed for the extension of the IRZ. As the IRZ decreases in width downstream from the inlet ($0.5d$), it reaches its minimum value at around $1.5d$ to $2d$, while the tangential velocity reaches its maximum value at this position. This effect could be attributed to the conservation of tangential momentum of the rotating motion of the fluid. Measured RMS values for the OXY21 case (cf. Figure 10b) of the tangential and axial velocity components have similar profiles as those obtained for the AIR case, but with higher values. Maximum RMS values of $RMS_u = 3.6$ m/s for the axial (at $H = 0.5d$) and $RMS_v = 2.2$ m/s (at $H = 1d$) for the tangential components were calculated. The turbulence levels in the OXY21 case, shown by the calculated RMS values, are about 1.7 times higher for the axial and 1.5 times higher for the tangential velocity components than those of the AIR case at the location of the maximum values.

Results obtained for the OXY25 case (cf. Figure 11) exhibit lower recirculation velocities (IRZ) than those found for the OXY21 case, but are higher than for the AIR case. Maximum values obtained are $\bar{u} = 8.0$ m/s (at $H = 0, 5d$) and $\bar{u} = -2.5$ m/s (at $H = 1d$). The extension of the IRZ is similar in width to the other two cases but the axial extension (in the direction of the symmetry axis of the chamber) lies in between the values found for the other two cases (AIR $H = 0.5d - 1.5d$ and OXY21 $H = 0.5d - 5d$). No negative axial velocity component values were measured at the location of the last profile ($H = 6d$). Tangential velocity component profiles show values in between the two cases (maximum is $\bar{v} = -3.4$ m/s at $H = 0.5d$). The maxima of the tangential velocity component remains
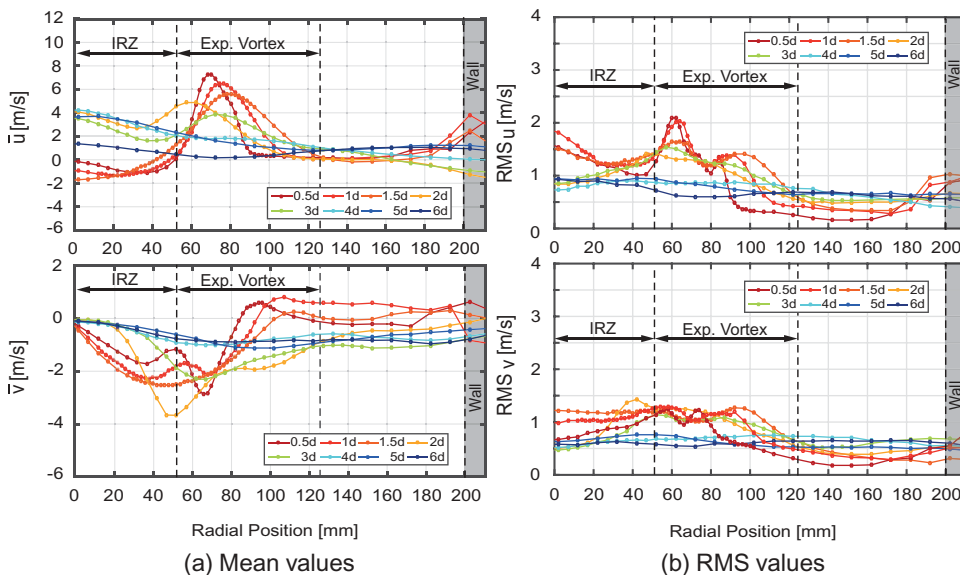

Figure 9. Measured LDV profiles of the axial (u) and tangential (v) velocity components for the AIR case: (a) mean values and (b) RMS values. Shaded regions represent measurements inside window ports.
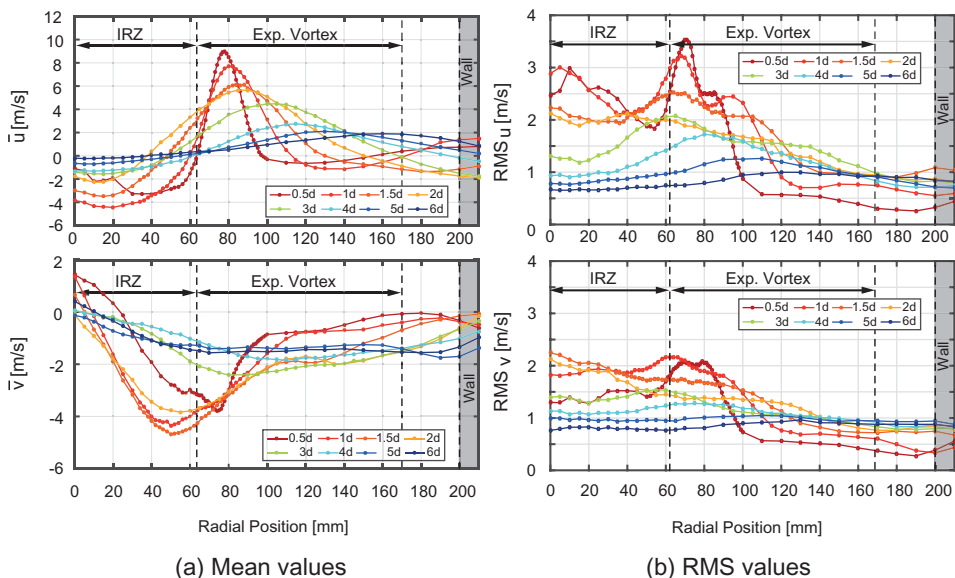
Figure 10. Measured LDV profiles of the axial (u) and tangential (v) velocity components for the OXY21 case: (a) mean values and (b) RMS values. Shaded regions represents measurements inside window ports.

in that order all the way down to $H = 2d$ to monotonically decrease and move towards the chamber walls as the profile relaxes further downstream. RMS values from the velocities show similar distributions as those from OXY21 but with rather lower values.
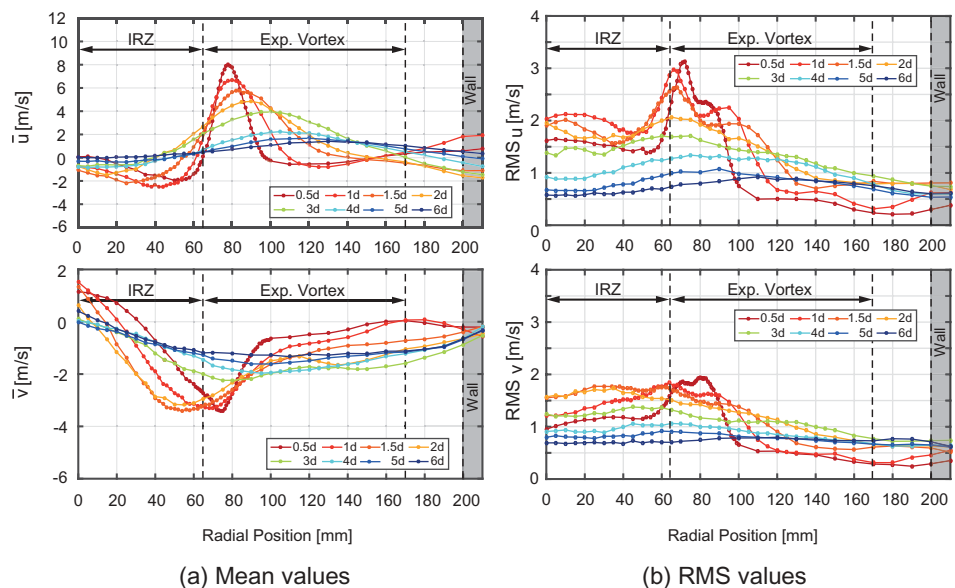

Figure 11. Measured LDV profiles of the axial (u) and tangential (v) velocity components for the OXY25 case: (a) mean values and (b) RMS values. Shaded regions represents measurements inside window ports.

Peak velocity RMS of the axial component are found in the vicinity of the peak corresponding to the maximum mean axial velocity (i.e., $R = 68$ mm at $H = 0.5d$), in the location of the highest gradients in the axial velocity component. As in the other studied cases, two RMS peaks can be seen in the proximity of the point maximum mean axial velocity, at the interface between the IRZ and the expanding vortex and at the outer side of the expanding vortex, at the interface with the flow at rest. Also, traces of an ERZ can be observed at the vicinity of the wall between $H = 1.5d$ and $H = 5d$. The profiles for OXY25 show a smooth evolution along the measured axial positions; flow relaxation can be seen by the broadening and decreasing peak values along the measured heights. The expansion of the vortex can be traced all the way down to $H = 6d$. As described above for the AIR case, the jets corresponding to the staging stream can also be measured near the burner port and the chamber walls for both OXY cases ($H = 0.5d$ to $H = 1.0d$ and between $R = 180$ mm and $R = 200$ m/s, with also $\bar{u} \approx 2$ m/s). Values from OXY cases show lower velocities given by the staging stream and could be attributed overall to the lower associated wall temperatures for these cases.

Flow fields from the three different pulverized coal swirl flames have shown all the typical features of swirling flows issuing from annular concentric nozzles with central nonswirling jets (Weber et al., 1990). The presence of internal and external recirculation regions, as well as the vortex structure development, is observed. Nevertheless, the impact of changing reactant composition when keeping the oxygen-fuel ratios constant is remarkable. The OXY21 case showed higher overall velocities in axial and tangential components as well as bigger IRZ and ERZ compared to the AIR case. The OXY25 case has also been shown to have higher overall velocities and more pronounced recirculation zones than the AIR case.

A previous study by Habermehl et al. (2016) reported that momentum fluxes have a significant influence on the flame structure. Momentum fluxes calculated for each of the streams are given in Table 1. Comparing bulk velocities and momentum fluxes for the OXY21 and AIR cases, the bulk gas injection velocities for the primary and secondary stream are identical and the ratio between secondary/primary flow at each case is constant ($U_{II}/U_I = 2.3$). The momentum flux of OXY21 is higher than the one from AIR, with corresponding momentum fluxes ratios of primary and secondary streams between the two cases (i.e, $U_{II,OXY21}/U_{II,AIR} = 1.35$, $U_{I,OXY21}/U_{I,AIR} = 1.36$). Thus, the higher measured velocities in OXY21 with respect to AIR can be attributed to the momentum increment introduced by replacing N_2 with CO_2 in the reactants. The higher velocities lead to higher turbulence levels (measured through the RMS values) in the flow, also a larger and more intense recirculation region is formed due to the higher velocities. This is a characteristic feature of swirling jets issued by annular concentric nozzles (Beér and Chigier, 1972).

Results obtained for the OXY25 case are located, regarding flow field patterns, in between those obtained for the AIR and the OXY21 flame, with overall velocities and turbulence intensities closer to those measured for OXY21. A particularly interesting observation arises when comparing the OXY25 case to the AIR case. As the local oxygen-fuel ratio is kept constant for the three cases, the volume flow, thus the injection velocity of the OXY25 case is reduced to compensate for the higher oxygen content of the reactants (and match the momentum of the OXY21 case), leading to lower bulk injection velocities at the secondary/primary streams as compared to AIR and OXY21 cases. Despite the lower velocities, measured velocity values in OXY25 follow very closely the values measured for OXY21.

An explanation for this can be found through results reported in previous works. Hees et al. (2016a) studied the structure of the three flames by imaging the spontaneous emission of OH* radicals, which allows to identify the regions featuring higher combustion activity. These results showed that OH* produced by the OXY25 flame was mostly located near the burner, indicating a compact flame region, or main reaction zone much closer to the burner than those for the OXY21 and AIR case. Later on, in a different study, the same authors (Hees et al., 2016b), performed measurements of CO and CO_2 gas concentrations inside the combustion chamber for the OXY21 and OXY25 case, where it was reported that CO and CO_2 gas concentrations were higher for OXY25 than for OXY21 in the near-burner regions ($H = 1d$ to $2d$), where the velocity peaks are located. CO concentrations were found further downstream to be close to zero. These parameters indicate that the flame for OXY25 ignites earlier and the oxidation reactions take place faster than for OXY21. Thus, the relatively higher velocities measured in the OXY25 case can be attributed to the acceleration of the bulk flow due to higher combustion activity near the burner where the fresh reactants penetrate into the combustion chamber.

The mean axial velocity component values measured at $H = 0.5d$ for all studied cases show values around zero in the IRZ, which could be associated with partial jet penetration (Chigier and Beer, 1964a). The smooth radial evolution of the mean axial and tangential velocity profiles in the oxy-fuel cases indicates that both the primary and secondary streams are fully merged at first measured axial position $H = 0.5d$. Becker et al. (2016) recently performed PIV measurements at intra-quarl regions in a dimensionally similar burner under oxy-fuel gas flames, and it was reported that the primary and secondary flows merge almost immediately after leaving the concentric annular nozzles (cf. Figure 3). On the other hand, the less smooth radial evolution of the tangential components observed in the AIR case (cf. Figure 9), particularly at $H = 0.5d$ and $H = 1d$ between $R = 40$ and $R = 60$ mm, could indicate that the primary and secondary are not yet fully merged at this position downstream from the burner.

Turbulent intensities measured on the flames are reported by the RMS values of the time velocity fluctuations measured by the LDV system. Obtained profiles showed that the OXY21 case features higher overall RMS values. The radial evolution of RMS profiles showed similar peak and gradient distributions for all studied cases. However, higher values were obtained for the axial component fluctuations than for the tangential component fluctuations in all cases (non-isotropic turbulence). Estimations of absolute total kinetic turbulent energy cannot be made, as no information about the radial velocity component was measured. However, the information obtained by the RMS values of the velocity fluctuations still gives an indication about the spatial distribution of turbulent kinetic energy. Both studied oxy-fuel cases showed higher RMS than the AIR case, being the OXY21 case producing the highest turbulence levels.

PIV velocity measurements and Mie scatter analysis

PIV measurements were performed at three different axial burner positions; velocity vector fields were computed using the measured axial and radial velocity components. Figure 12 shows PIV measurement results (concatenated) for the three cases. The color scale in Figure 12 represents the magnitude of the velocity vector composed by the measured axial and radial velocity components. Obtained vector fields show, with a higher
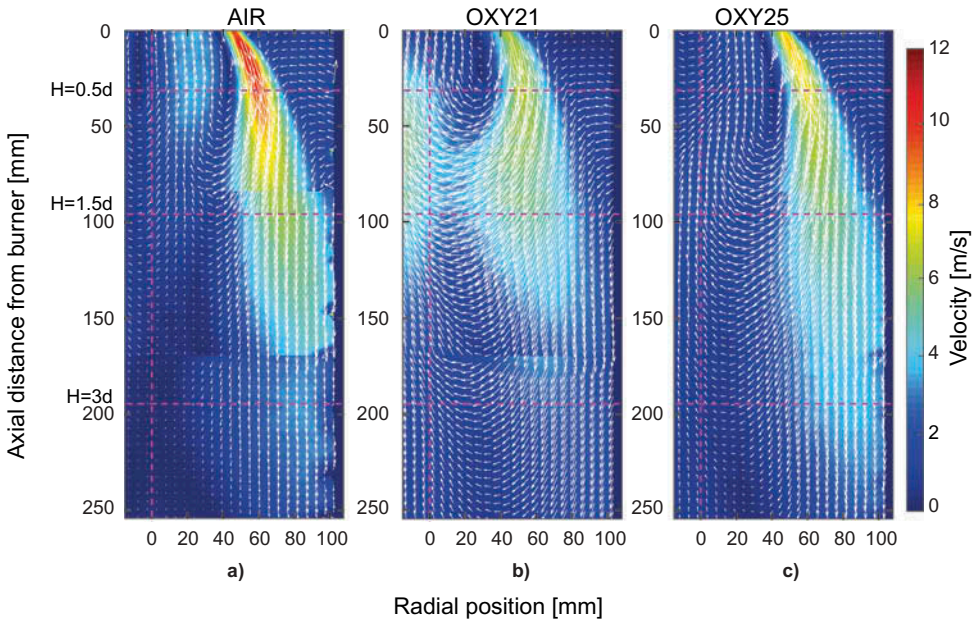
Figure 12. Two-dimensional velocity fields obtained from PIV measurements of AIR, OXY21, and OXY25 case. Horizontal dotted lines correspond to the position of the measured 0.5d, 1.5d, and 3d LDV profiles.

level of detail, the differences described in the previous subsection from the LDV results. The expanding vortex and the IRZ can be clearly identified for the three cases. The ERZ cannot be observed as the view angle of the laser sheet through window no. 2 (cf. Figure 8) is not wide enough to image the radial positions between $R = 100$ mm to 200 mm. In return, PIV can measure velocities all the way up to the dump plane and also provides information about the radial velocity components, which the LDV system cannot directly provide.

Figure 12a shows the obtained vector fields for the AIR case. The expansion behavior of the swirling vortex and the IRZ can be identified and analyzed. As it was already observed in the LDV measurements, the IRZ is less intense in the AIR case than for OXY21 or OXY25. Figure 13 shows the mean axial velocity component profiles, which were extracted at $H = 0.5d$, 1.5d, and 3d from the PIV results compared to the corresponding profiles measured by LDV. Comparing the PIV and LDV profiles on Figure 13a, velocities measured by the two techniques show considerable differences, particularly at the region of the main swirling jet ($R = 70$ mm) and inside the IRZ ($R = 0$ mm). These differences are smaller for positions further downstream and away from the center of the chamber. Also, velocities measured in the near-burner region ($H = 0$ to 50 mm) exceeded those measured for the other two cases, with values close to the calculated bulk injection velocities at the secondary stream (cf. Table 1).

Figure 12b shows results for the OXY21 case. A more intense and extended IRZ is observed in the vector fields, also consistent with the observed results from the LDV measurements. The expanding vortex shows a strong flow deviation towards the IRZ, a
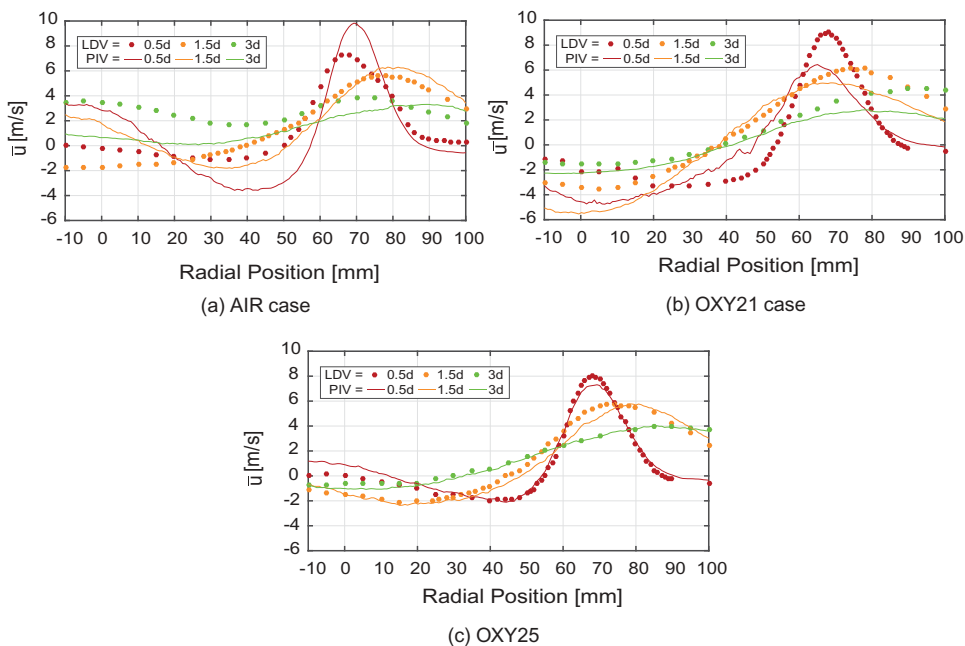
Figure 13. Comparison between LDV and PIV results, mean axial velocity component at three different axial positions.

feature undetected by the LDV measurements, which is not as significant in the other two cases. The values of the mean axial velocity components from PIV also differ from the LDV results (cf. Figure 13b), especially for the profile at $H = 0.5d$, where the peak velocity ($R = 70$ mm) is estimated by PIV to be lower than the one measured by LDV. Values measured at the IRZ also differ from the LDV measurements; the PIV measurements show higher velocities at the IRZ. As observed in the AIR case, the differences between the PIV and LDV profiles get smaller for the profiles further downstream. Figure 12c shows the PIV results from the OXY25 case, the vector fields also show a smooth evolution of the expanding vortex, featuring a less intense recirculation zone, with similar dimensions to the one of the OXY21 case; The vortex in OXY25 does not show the strong velocity shift towards the center as it was observed for OXY21. Here, it expands and velocities decay towards the walls of the combustion chamber. A comparison against LDV data (cf. Figure 13c) shows much better agreement between the two measurement techniques than for the two other cases. PIV mean axial slightly deviates from the LDV measurements towards the center of the IRZ and at the point of maximum velocity in the expanding jet (at $H = 0.5d$ at $R \approx 70$ mm). PIV profiles at $H = 1.5d$ and $3d$ show very small differences compared to those given by the LDV.

Possible causes for the observed differences between PIV and LDV profiles can be attributed to different factors: (i) PIV image pairs from regions in the flame with high particle density lead to high noise levels, which renders a high number of spurious vectors. These calculated spurious vectors are rejected during the post processing leaving gaps in the vector fields. As mentioned in the "particle image velocimetry" section, only around 30% of the useful vectors are taken into account for the computation of the PIV mean and

RMS values. The calculated mean velocity values do not include the events of the dense particle clouds. Therefore, the mean velocities are biased and thus differ from the measured LDV values. (ii) The larger particles produce the highest correlation peaks during the cross-correlation analysis of the PIV image pairs. Therefore, the PIV processing algorithms are biased towards producing velocity vectors given by the larger particles (Balusamy et al., 2013). A close inspection of individual PIV image pairs shows that the larger particles, which are subjected to higher slip, tend to move downwards in the IRZ in all three cases. Thus, the observed individual larger particles do not follow, in most cases, the direction of the smaller particles located in their vicinity. Therefore, the observed differences between LDV and PIV measurements can be attributed to a combination of high-density particle clouds noise and the velocity bias introduced by the large particles, which distort the velocity vector determination from PIV cross-correlation analysis.

In order to quantify the spatial particle distributions, instantaneous Mie scatter images from each studied case were averaged (Figure 14, average of 1000 frames) and concatenated in a similar way to the vector fields shown in Figure 12. The resulting concatenated images from the Mie scattering given by the coal particles show significant differences in the spatial distribution of the particles and in the scattering intensities between the three cases. In the AIR case (cf. Figure 14a), most of the particles are located in a compact region near the center of the combustion chamber and the intensity values are considerably higher than those in the oxy-fuel cases. In the OXY21 case (cf. Figure 14c), particles are mostly located along the expanding vortex and they provide the lowest scattering intensity values of all three cases. The OXY25
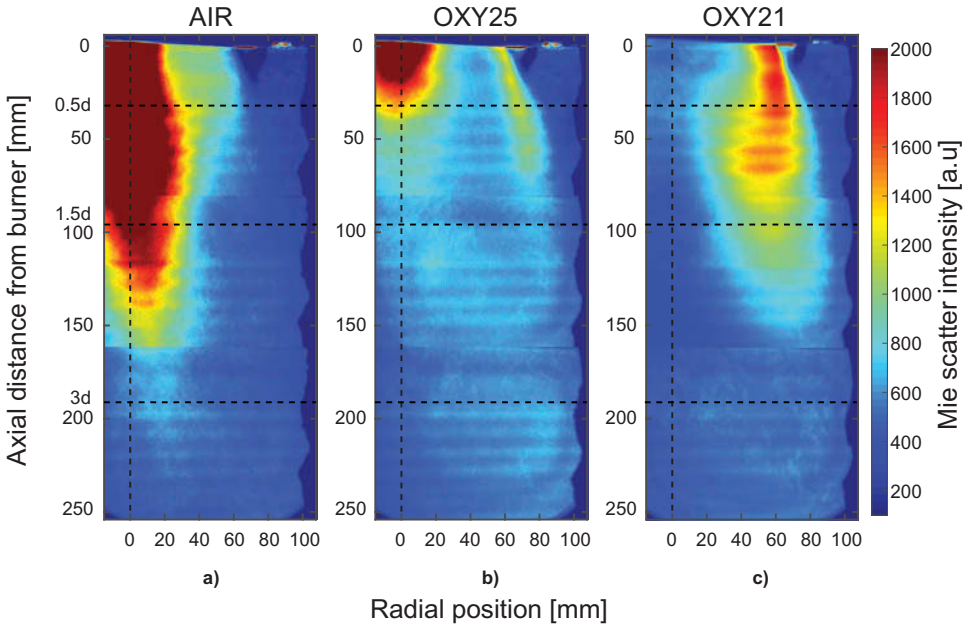

Figure 14. Mie scattering of the laser sheet by the solid particles in the flame, for all three studied conditions. For comparison purposes color maps are limited to 2000 [$a.u.$], thus the center regions on (a) and (b) are deliberately saturated. Horizontal dotted lines correspond to the position of the measured 0.5d, 1.5d, and 3d LDV profiles.

case (cf. Figure 14b) shows what could be an intermediate stage between the AIR and OXY21 case. The observed disparity of the particle distribution between air and oxyfuel cases can be explained by the different aerodynamic drag of the particles in the different atmospheres. When judging the aerodynamic quality of tracer particles, a Stokes flow around the particle is usually assumed. In a Stokes flow the aerodynamic drag of a sphere, is given by Stokes law: $F_d = 6\pi\mu rs$, where F_d represents the drag force, μ the dynamic viscosity, r the radius of the sphere, and s the slip velocity. Here, the fluid affects the drag only by its viscosity but not by its density. The assumption of a Stokes flow around the particle is considered to be valid if $S_k < 0.1$. The majority of the used coal particles in the used configuration, however, have a higher Stokes number ("Particle slip velocity error" section). For larger and faster objects, the aerodynamic drag is given by the drag equation: $F_d = 0.5\rho s^2 C_D A$. Here, ρ represents the density of the fluid, C_d the drag coefficient, and A the reference area. In this case the fluid affects the drag by its density. The higher densities of the oxy-fuel atmospheres induce a higher drag on the particles. Hence, the particles are less likely to move against the flow and penetrate the IRZ in the oxy-fuel cases.

Another interesting feature arising from the Mie scattering averaged images is that the AIR case gives far higher scattering intensities than the other two cases (in Figure 12, the color scale is mostly saturated at the high intensity regions, with values reaching up to 8000). Particles entering the combustion chamber following the edge line of the quarl, which is a region with higher oxygen concentration, might burn faster (decreasing their scattering signature). The opposite takes place in the IRZ; the lower oxygen concentration might lead to slower combustion rates for the particles, which, combined with the near stagnating velocities, could lead to particle accumulation effects.

Conclusions

Flow fields from three different pulverized 60-kW swirl coal flames were studied by means of nonintrusive laser diagnostic techniques. Two-component LDV measurements were complemented by measurements PIV. LDV measurements of mean velocity components (axial and tangential) as well as the corresponding RMS values of each measured point were presented with high spatial and temporal resolution. Obtained results from LDV and PIV measurements are presented and discussed in detail to explain the observed aerodynamic effects introduced by the different operating conditions.

LDV measurements of the oxy-fuel cases (OXY21 and OXY25) show that both have overall higher velocities as well as much stronger recirculation zones than the reference AIR case. Higher turbulence was also observed (indicated by the RMS values) for the oxy-fuel cases. In all three cases, turbulence was measured to be nonisotropic, with the highest values at the IRZ and in the strain layers located at the internal and external boundaries of the expanding vortex.

Complementary PIV measurements provided valuable data allowing the flow field analysis to be made with greater detail. The 2D velocity vector fields from PIV served to extend the observations from the LDV measurements, in particular the extension of the IRZ and the radial evolution of the expanding vortex flows. Nevertheless, it was observed that the estimated values of the axial velocity components given by PIV deviate from LDV results in the regions with high particle loads. In addition, the velocities of larger and

smaller particles, accounted for in the cross-correlation analysis, had also a negative impact on the PIV velocity measurements. To detect and exclude the larger particles in the post-processing might help overcome the latter problem (Balusamy et al., 2013). To address the issue of high particle load in the flow, some of the small particles could be removed. However, this can be difficult in large facilities, and it can modify the present flames in a way that they are no longer comparable. In spite of that, double frame Mie scatter images are valuable as they provide qualitative information about solid particle distributions in the flame.

The analysis of Mie scattering images have shown that in the three studied cases, particles are distributed in a fairly different way. In the AIR case, particles are mostly confined around the center of the combustion chamber, while in the OXY21 case particles are carried out by the swirling secondary stream and enter the combustion chamber following the edge line of the quarl. The OXY25 case showed a mid-point distribution, with particles at the center near the burner and also entering the chamber as observed in OXY21 case.

The combined analysis of measured flow fields and Mie scattering images indicate that in the oxy-fuel cases, the higher flow velocities and the different thermophysical properties of the reactants (in particular the higher density), might enhance the aerodynamic drag upon coal particles when compared to the AIR case. This higher aerodynamic drag in the two oxy-fuel cases allows more coal particles to be carried away by the swirling secondary flow. Nevertheless, further investigations are required to clearly identify and understand the factors that lead to the different coal particle distributions in the studied cases.

Acknowledgments

Funding

ORCID

D. Zabrodiec 🔟 http://orcid.org/0000-0001-7611-6403

References

Abbott, M.P. 1989. Two phase velocity and turbulence measurements in a 0.5 mw pulverized coal fired furnace. Presented at the 9th IFRF Members' Conference, Noordwijkerhout, the Netherlands, May 24–26.

Abraham, B., Asbury, J., Lynch, E., and Teotia, A. 1982. Coal-oxygen process provides CO_2 for enhanced recovery. *Oil Gas J.*, **80**(11), 68–75.

Albrecht, H.E., Borys, M., Damaschke, N., and Tropea, C. 2003. *Laser Doppler and Phase Doppler Measurement Techniques*, Springer, Berlin.

Andersson, K., and Johnsson, F. 2007. Flame and radiation characteristics of gas-fired O_2/CO_2 combustion. *Fuel*, **86**, 656–668.

Balusamy, S., Schmidt, A., and Hochgreb, S. 2013. Flow field measurements of pulverized coal combustion using optical diagnostic techniques. *Exp. Fluids*, **54**, 1–14.

Becker, L.G., Kosaka, H., Böhm, B., Doost, S., Knappstein, R., Habermehl, M., Kneer, R., Janicka, J., and Dreizler, A. 2016. Experimental investigation of flame stabilization inside the quarl of an oxyfuel swirl burner. *Fuel*, **201**, 124–135.

Béer, J.M., and Chigier, N.A. 1972. *Combustion Aerodynamics*, Applied Science Publishers LTD, London.

Chen, L., Yong, S.Z., and Ghoniem, A.F. 2012. Oxy-fuel combustion of pulverized coal: Characterization, fundamentals, stabilization and CFD modeling. *Prog. Energy Combust. Sci.*, **38**, 156–214.

Chigier, N., and Beer, J. 1964a. The flow region near the nozzle in double concentric jets. *J. Basic Eng.*, **86**, 797–804.

Chigier, N., and Beer, J. 1964b. Velocity and static-pressure distributions in swirling air jets issuing from annular and divergent nozzles. *J. Basic Eng.*, **86**, 788–796.

Croiset, E., Douglas, P., and Tan, Y. 2005. Coal oxyfuel combustion: A review. Presented at the 30th International Conference on Coal Utilization and Fuel Systems, Clearwater, FL, April 17–21.

Cuéllar-Franca, R.M., and Azapagic, A. 2015. Carbon capture, storage and utilisation technologies: A critical analysis and comparison of their life cycle environmental impacts. *J. CO2 Util.*, **9**, 82–102.

El Gendy, H., Preciado, I., Ring, T., and Eddings, E. 2010. Particle image velocimetry of pulverized oxy-coal flames. Presented at the 2010 AIChE Annual Meeting, Salt Lake City, UT, November 7–12.

Ereaut, P., and Gover, M. 1991. LDA measurements of flame velocities at a 2000 MWE coal-fired power station. *J. Inst. Energy*, **64**, 135–142.

Fielenbach, C., Holfeld, T., von Petery, C., Renz, U., and Wnning, J. 2003. NOx-reduction in a pressurized pulverized coal flame by flue gas recirculation. Presented at the 20th International Pittsburgh Coal Conference, Pittsburgh, PA, September 15–19.

Habermehl, M., Hees, J., Massmeyer, A., Zabrodiec, D., Hatzfeld, O., and Kneer, R. 2016. Comparison of flame stability under air and oxy-fuel conditions for an aerodynamically stabilized pulverized coal swirl flame. *J. Energy Res. Technol.*, 138.

Habermehl, M., Toporov, D., Erfurth, J., Frster, M., and Kneer, R. 2012. Experimental and numerical investigation on a swirl oxycoal flame. *Appl. Therm. Eng.*, **49**, 161–169.

Hees, J., Zabrodiec, D., Massmeyer, A., Habermehl, M., and Kneer, R. 2016a. Experimental investigation and comparison of pulverized coal combustion in CO_2/O_2 and N_2/O_2 atmospheres. *Flow Turbul. Combust.*, **96**, 417–431.

Hees, J., Zabrodiec, D., Massmeyer, A., Pielsticker, S., Gövert, B., Habermehl, M., Hatzfeld, O., and Kneer, R. 2016b. Detailed analyzes of pulverized coal swirl flames in oxy-fuel atmospheres. *Combust. Flame*, **172**, 289–301.

Heil, P., Toporov, D., Stadler, H., Tschunko, S., Frster, M., and Kneer, R. 2009. Development of an oxycoal swirl burner operating at low O_2 concentrations. *Fuel*, **88**, 1269–1274.

International Energy Agency (IEA). 2016. *Coal Information 2016*, International Energy Agency, Paris, France.

Jensen, P., Ereaut, P., Clausen, S., and Rathmann, O. 1994. Local measurements of velocity, temperature and gas composition in a pulverised-coal flame. *J. Inst. Energy*, **67**, 37–46.

Leuckel, W., and Fricker, N. 1976. Characteristics of swirl-stabilized natural-gas flames. Part 1: Different flame types and their relation to flow and mixing patterns. *J. Inst. Fuel*, **49**, 103–112.

Leung, D.Y., Caramanna, G., and Maroto-Valer, M.M. 2014. An overview of current status of carbon dioxide capture and storage technologies. *Renewable Sustainable Energy Rev.*, **39**, 426–443.

Liu, H., Zailani, R., and Gibbs, B. 2005. Comparisons of pulverized coal combustion in air and in mixtures of O_2/CO_2. *Fuel*, **84**, 833–840.

Nobach, H. 2001. LDA benchmark generator iii. Available at: http://ldvproc.nambis.de/programs/bm3.html.

Pickett, L.M., Jackson, R.E., and Tree, D.R. 1999. LDA measurements in a pulverized coal flame at three swirl ratios. *Combust. Sci. Technol.*, **143**, 79–107.

Pope, S. 2000. *Turbulent Flows*, Cambridge University Press, New York.

Pröbstle, G., and Wenz, W. 1988. Velocity measurements in a swirl driven pulverized coal combustion chamber. *Combust. Flame*, **72**, 193–203.

Scheffknecht, G., Al-Makhadmeh, L., Schnell, U., and Maier, J. 2011. Oxy-fuel coal combustion: A review of the current state-of-the-art. *Int. J. Greenhouse Gas Control*, **5**(Suppl 1), S16–S35.

Schnell, U., Kaess, M., and Brodbek, H. 1993. Experimental and numerical investigation of NOx formation and its basic interdependences on pulverized coal flame characteristics. *Combust. Sci. Technol.*, **93**, 91–109.

Silva, R.C.D., Kangwanpongpan, T., and Krautz, H.J. 2014. Flame pattern, temperatures and stability limits of pulverized oxy-coal combustion. *Fuel*, **115**, 507–520.

Sung, Y., Lee, S., Eom, S., Moon, C., Ahn, S., Choi, G., and Kim, D. 2016. Optical nonintrusive measurements of internal recirculation zone of pulverized coal swirling flames with secondary swirl intensity. *Energy*, **103**, 61–74.

Toporov, D., Bocian, P., Heil, P., Kellermann, A., Stadler, H., Tschunko, S., Frster, M., and Kneer, R. 2008. Detailed investigation of a pulverized fuel swirl flame in CO_2/O_2 atmosphere. *Combust. Flame*, **155**, 605–618.

Tropea, C., Yarin, A., and Foss, J.F. (Eds.) 2007. *Springer Handbook of Experimental Fluid Mechanics*, Springer Verlag, Berlin.

Wall, T., Liu, Y., Spero, C., Elliott, L., Khare, S., Rathnam, R., Zeenathal, F., Moghtaderi, B., Buhre, B., Sheng, C., Gupta, R., Yamada, T., Makino, K., and Yu, J. 2009. An overview on oxyfuel coal combustion—State of the art research and technology development. *Chem. Eng. Res. Des.*, **87**(8), 1003–1016.

Wang, C., Berry, G., Chang, K., and Wolsky, A. 1988. Combustion of PC using waste carbon dioxide and oxygen. *Combust. Flame*, **72**, 301–310.

Weber, R., Dugué, J., Sayre, A., and Visser, B. 1992. Quarl zone flow field and chemistry of swirling pulverized coal flames: Measurements and computation. *Symp. (Int.) Combust.*, **24**, 1373–1380.

Weber, R., Visser, B., and Boysan, F. 1990. Assessment of turbulence modeling for engineering prediction of swirling vortices in the near burner zone. *Int. J. Heat Fluid Flow*, **11**, 225–235.

Weidmann, M., Verbaere, V., Boutin, G., Honor, D., Grathwohl, S., Goddard, G., Gobin, C., Dieter, H., Kneer, R., and Scheffknecht, G. 2015. Detailed investigation of flameless oxidation of pulverized coal at pilot scale (230 kw). *Appl. Therm. Eng.*, **74**, 96–101.